ARTICLE

Check for updates

Gradient droplet distribution promotes spontaneous formation of frost-free zone

Chenguang Lu [1], Cong Liu[1], Zichao Yuan[1], Haiyang Zhan[1], Danyang Zhao[1], Lei Zhao[1], Shile Feng[1] & Yahua Liu [1]✉

The inhibition of condensation frosting at harsh environments is critical in various anti-icing applications. However, frosting on the entire surface is the final fate for most passive anti-icing strategies as a result of inevitable ice nucleation of subcooled droplets from the surface edges or defects and the following inter-droplet freezing wave propagation. Here, we report the frost-free zone formation on a macro-ridged surface. We design a macroscale ridge on the surface and show that this surface configuration changes the spatial distribution of water vapor diffusion flux during the condensation stage, resulting in a gradient arrangement of condensate droplets according to their size. This allows numerous failures of local inter-droplet ice bridging in the area with a critical droplet coverage rate, which triggers the interruption of the global freezing wave propagation and the evaporation of the rest droplets to form a frost-free zone around the ridge corner. These findings extend our understanding of frost formation on the surface and provide a rationale for the surface design with impressive durable anti-frosting performance.

[1] Key Laboratory for Precision & Non-traditional Machining Technology of Ministry of Education, Dalian University of Technology, Dalian 116024, PR China.
✉email: yahualiu@dlut.edu.cn

ce and frost accumulating on surfaces is ubiquitous in nature and our daily life, which also threatens the safe and efficient operation of transportation and energy infrastructure such as aircrafts, marine vessels, wind turbines and power transmission lines[1–3]. Traditional strategies for anti-icing and deicing, including electrothermal heating, chemical deicing fluids and mechanical removal, are usually energy consuming, environmentally hazardous and inefficient. Therefore, extensive attention has been devoted to passive anti-icing approaches with the capability to inhibit ice formation before freezing and meanwhile facilitate ice removal after freezing without external energy input[4–11]. In an ideal case, superhydrophobic textured surfaces with an extreme water-repellent property show great potential in passive anti-icing. However, the random nucleation of condensed droplets within the micro/nano-textures under high humid conditions leads to the collapse of the superhydrophobic state of the surface, due to the undesired Cassie-to-Wenzel transition[12–14]. Alternatively, slippery liquid-infused porous surfaces rendered remarkable freezing delay and ultralow ice adhesion, which are attributed to the molecular smoothness of the surface and low contact angle hysteresis after lubricant infusing within the textures[15–18]. Nevertheless, the lubricant both spreading over the condensed and frozen droplets suffers from great mass loss when the droplets shed off the surface[19,20]. In addition, once ice crystals generated due to defects[16,21,22], contaminations[23] or unsaturated gas flow[24], frosting continuously on the surface because of inter-droplet freezing wave propagation is the final fate for most of the passive anti-icing surfaces[25–27].

Studies have shown that inter-droplet ice bridging accounts for continuous frost coverage due to its propagation in a chain reaction fashion[21,22,28,29]. The corresponding microscopic mechanism is the hygroscopicity of ice arising from the localized vapor pressure gradient, which is formed by the depressed saturation vapor concentration of ice with respect to supercooled droplet at the same temperature[30,31]. The vapor pressure gradient drives water molecules evaporated from supercooled droplet to deposit on the ice, which constitutes the outstretched ice bridge. Consequently, the adjacent liquid droplet will be connected by the ice bridge successfully and frozen to ice before evaporating completely[21,29]. Although the hygroscopicity of ice can promote the propagation of freezing wave, it can also be utilized to suppress continuous coverage of frost by constructing patterned sacrificial ice stripes, such as microgrooves with prestored frozen water[32], patterned stripes with ice nucleating proteins[33] and patterned polyelectrolyte coatings[34]. Owing to a depressed saturation vapor pressure over ice, these sacrificial ice stripes serve as humidity sinks which can siphon vapor from surroundings to keep the rest of the substrate frost free. A similar effect was observed in the scaleup serrated structure with a frost-free zone in the valley[35]. However, most of the above research is focused on the validation of surface anti-icing performance whereas the underlying mechanism are rarely touched, which restricts its development and widespread application.

In this study, we report a new strategy that allows for the interruption of continuous frost coverage, endowing the frost-free zone formation. A surface with a millimeter-scale ridge was fabricated to generate a gradient distribution of condensate droplets, which leads to numerous failures of ice bridge connection at the area with a critical droplet coverage rate. We show that the interruption of the consecutive freezing wave propagation synergized with drop evaporation for the hygroscopicity of ice, resulting in the establishment of a stable frost-free zone on both sides of the ridge over 48 hours.

Results and discussion
Condensation frosting on the macro-ridged surface.
Macro-ridged surfaces of height H and width D (Fig. 1a) were fabricated

using a wire cutting machine, followed by magnetic grinding to achieve a surface roughness of ~0.3 μm and a water contact angle of ~100° (Supplementary Fig. 1 and Fig. 1b). The roughness, contact angles, and advancing/receding angles of various surfaces are listed in Supplementary Table 1. The condensation frosting experiments were carried out in a chamber with controlled temperature and humidity (the schematic diagram is shown in Fig. 1c). The ambient and surface temperature were set at $T_{air} = 20 \pm 0.5\,°C$ and $T_w = -7 \pm 0.2\,°C$, respectively. Meanwhile, the ambient relative humidity (RH) is controllable to sustain a supersaturation level defined as $S = RH \cdot P_{air}/P_w$, where P_{air} is the saturation pressure for water vapor at T_{air}, and P_w is the saturation vapor pressure of supercooled water at T_w[31,32,36]. Detailed information about sample preparation is described in the Methods section and the surface temperature calibration is presented in Supplementary Note 1.

Figure 1d shows selected time-lapse images of condensation frosting on a flat surface at supersaturation level $S = 2$. The water vapor first condensed into relatively uniform droplets (shown as the inset at $t = 30\,s$), followed by rapid propagation of freezing wave ($t = 360\,s$) initiating from the sample edges, and finally the whole surface was covered by dense frost ($t = 3600\,s$). Note that, the freezing wave propagation can be clearly observed owing to the different refractive indices of light in water and ice (Supplementary Movie 1). However, a totally different scene is found during the condensation frosting on a macro-ridged surface, e.g., $H = 3$ mm and $D = 1$ mm (abbreviated as H3D1), at the same supersaturation level $S = 2$ (Supplementary Movie 2). Specifically, at the condensation stage, e.g., $t = 100\,s$ in Fig. 1e, the condensation droplets on the surface distributed in a gradient manner, with the bigger ones farther away from the ridge, as verified by the drop distribution in an enlarged view in Fig. 1f. Note that, the largest droplets located on the top of the ridge (inset in Fig. 1e), which phenomenon is consistent with previous research[37]. Then ice crystals formed preferentially on the edges (defects) of the surface, followed by the freezing wave propagation as indicated by the white dotted line at $t = 980\,s$ in Fig. 1e. As the freezing wave advancing, interestingly, an evaporation wave indicated by the yellow dotted line emerged due to the water droplet evaporation (Supplementary Note 2). The concurrent icing and evaporating for water droplets are in the following termed multi-phase transition. Finally, a symmetric frost-free zone formed on both sides of the ridge and kept stable for a long time, e.g., $t = 3600\,s$. The whole condensation frosting process on the macro-ridged surface is depicted in Fig. 1g, with clearly identified three stages including droplet condensation, multiphase transition and final formation of frost-free zone.

Droplet condensation.
To better elucidate the formation and evolution of the frost-free zone, we first deliberate on the droplet condensation process. As discussed above, it is obvious that the millimeter-scale ridge modified the distribution of condensate droplets compared to that on a flat surface. To interpret the difference, we numerically simulated the diffusion behavior of water vapor over the macro-ridged surface, given that water vapor in ambient environment is the source of condensates. Figure 2a shows the boundary conditions. Since the experiment was carried out in a chamber without disturbing the airflow, the assumption that condensation occurred at a steady state in a diffusion boundary layer is acceptable, indicating that the mass transfer mainly occurs through water vapor diffusion[38,39]. The thickness of the boundary layer ζ is estimated to be ~1 cm according to previous research[32,39]. The concentration of water vapor in ambient is set as $c_0 = 0.298$ mol m^{-3} with the ambient temperature $T_{air} = 20\,°C$ and relative humidity $RH = 31\%$. The c_w defined as the equilibrium
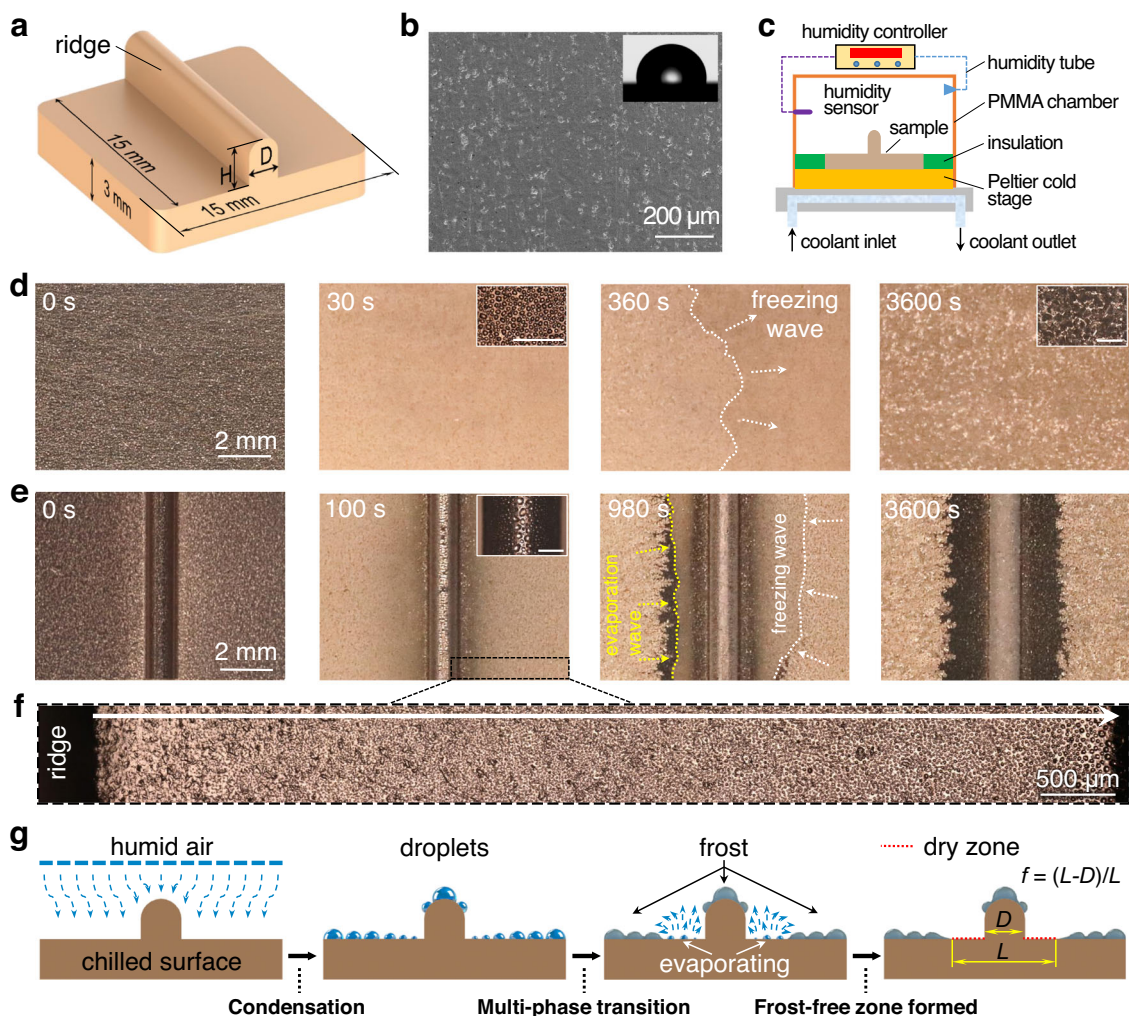
Fig. 1 Condensation frosting on the surface. a Schematic showing the parameters of the macro-ridged surface. **b** Scanning electronic micrograph (SEM) image of the surface. The inset shows a contact angle of ~100° with a 3 μL drop. **c** Schematic showing the setup for condensation frosting experiments. **d** Condensation frosting on a flat surface. The insets show the high magnification optical images of the condensates at 30 s and frost at 3600 s, respectively. Scale bar, 300 μm. **e** Condensation frosting on the macro-ridged surface H3D1. The inset shows the high magnification optical image of droplets on the top of ridge at 100 s. White dotted line indicates the propagation of freezing wave and yellow dotted line indicates evaporation wave in the multi-phase transition stage. Scale bar, 300 μm. **f** Gradient distribution of condensate droplets on the macro-ridged surface. **g** Schematic showing the frost-free zone formation at different stages on a macro-ridged surface.

vapor concentration of subcooled water at the substrate temperature $T_w = -7\,°C$ is set to be 0.163 mol m^{-3}. The detailed calculation of c_0 and c_w is given in Supplementary Note 3.

Numerical calculation results in Fig. 2b displayed the spatial distribution of diffusion flux on the ridge and the surrounding flat regions. As indicated by the color gradient from red to blue, the diffusion flux intensity of water vapor is maximal on top of convex ridge while minimal at its corner. A higher intensity of diffusion flux means a faster mass transfer of the water vapor, which corresponds to more water molecules gathered. This is verified by the size distribution that more big droplets condense on the top of the ridge than that on the flat region, as shown at $t = 100$ s in Fig. 1e. To interpret the gradient arrangement of condensate droplets on the surface shown in Fig. 1f, the numerical solution of diffusion flux over the macro-ridged surface was plotted in Fig. 2c with black solid line, which shows a good agreement with the trend of the droplet coverage rate (red circles, the data extraction is discussed in the Methods part) obtained from the experiments. Here, the droplet coverage rate φ is defined as the ratio of the droplet-covered area to the whole

surface area. Note that, the droplet coverage rate over the macro-ridged surface at different time experiences a similar variation tendency, as evidenced by Supplementary Fig. 3, with a lower φ close to the ridge corner due to the low diffusion flux.

Multi-phase transition. Unlike the macroscopic phenomenon that only single freezing wave propagates on a flat surface, e.g., at $t = 360$ s in Fig. 1d (Supplementary Movie 1), evaporation wave initiates after the freezing wave terminates and propagates along the surface (yellow dashed line in Supplementary Fig. 4 and Supplementary Movie 2), indicating that both liquid-to-solid and liquid-to-gas phase transitions occurred on the macro-ridged surface. The liquid-to-solid phase change originally arises from ice nucleation at the surface edges or defects, followed by inter-droplet ice bridge connection in a chain reaction manner, which is visually manifested by freezing wave propagation in Supplementary Movie 3. However, the obviously observed liquid-to-gas phase change of the droplets, i.e., the widespread droplet evaporation around the ridge corner, always starts after ice is formed (Supplementary Movie 2), which implies that the formation of ice
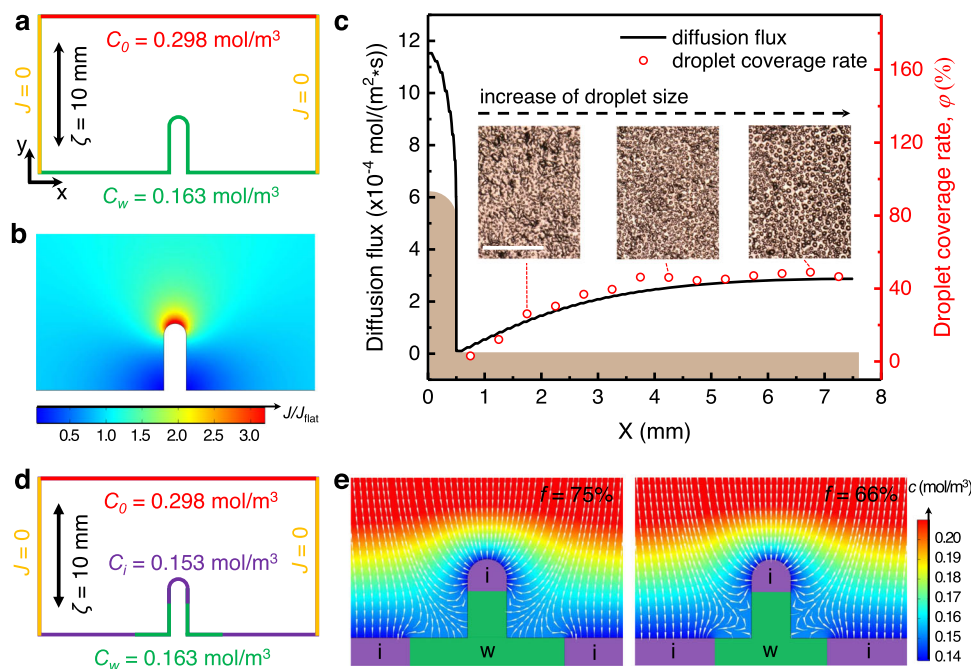
Fig. 2 Vapor diffusion over a macro-ridged surface during condensation frosting. a Boundary conditions for simulating condensation process.
b Numerical calculation of the total vapor diffusion flux over the macro-ridged surface J normalized by that on a flat surface J_{flat} at a steady state during condensation stage (Supplementary S3). **c** Distribution of vapor diffusion flux and the droplet coverage rate (Supplementary Fig. S5) on the macro-ridged surface. The insets show the corresponding micrographs related to the data points. Scale bar, 300 μm. **d** Boundary conditions for simulating the droplet evaporation. **e** Diffusion flux on the macro-ridged surface H3D1.5 with $f = 75\%$ and 66%, respectively. The arrows indicate the directions of vapor flux.

zones has changed the nearby diffusion behavior of vapor. To give a clear explanation of this phenomenon, we use the boundary conditions to simulate the droplet evaporation. As shown in Fig. 2d, the purple regions represent the ice zones, and the concentration of water vapor over the ice zones is set as $c_i = 0.153$ mol m^{-3} by using the ideal gas law with the equilibrium vapor pressure of ice at the surface temperature $T_w = -7\,°C$ and the detailed information is give in Supplementary Note 3. The selection of the purple regions is consistent with the ice distribution on the macro-ridged surface in the experiment, as shown in Supplementary Fig. 5. Figure 2e shows the vapor diffusion flux represented by the streamlines on the surface at two different frost-free area proportion (defined as $f = (L - D)/L$ as shown in Fig. 1g). The arrowheads indicate the motion direction of water vapor, and the color shading represents the concentration field of the water vapor. At a large frost-free area proportion, e.g., $f = 75\%$, water vapor diffuses onto the water region (denoted by "w"), which means the droplets around the corner are being continuously fed and keep growing (left in Fig. 2e). In other words, evaporation in the water region would not occur when $f \geq 75\%$. After a parametric sweep of f with a minimal step, a critical value $f^* \approx 66\%$ is found, under which the droplets in the water region evaporate completely. As shown in the right panel of Fig. 2e, water vapor diffuses out from the water region and onto the ice region (denoted by "i"), implying that the droplets near the ridge corner undergo a continuous and fast evaporation until the dry-zone is formed. Therefore, the dry-zone formation is determined by the competition between the incoming flux from ambient to the water region and the outgoing flux from the water region to the ice region, namely, dry-zone formed when the latter dominated, e.g., at the critical condition $f^* \approx 66\%$.

Frost-free zone formation. The above simulations explained how the ice region affected the water evaporation from a macroscopic perspective. However, the inter-droplet ice bridging process is not

taken into consideration, namely, the microscopic mechanism for the boundary formation to separate the frost-free and ice region is still elusive. To provide insight into this point, the evolution and formation of frost-free region is studied with more details. At the time point t_1 in Fig. 3a, the ice region (right side as separated by the white dotted line) can be easily identified by the irregular angular outline of the frozen droplets, which are closely linked to each other. Then part of the droplets (left side as separated by the white dotted line) survive from freezing and evaporate, which is manifested by the propagation of evaporation wave, as indicated by the traveling of the green dotted line from $t_1 + 18$ s to $t_1 + 96$ s in Fig. 3a and Supplementary Movie 4. Note that, this fast droplet evaporation suppresses the inter-droplet ice bridging and a close look at the failure of ice bridge connection is shown in Fig. 3b, where droplets circled by red curves are connected by ice bridge while droplets circled by yellow ones evaporated due to the failure of ice bridge connection. Undoubtedly, numerous failures of ice bridging that occurred intensively on the macro-ridged surface accounts for the dry zone formation (Supplementary Fig. 8). As a result, the consecutive propagation of ice bridge is interrupted thoroughly, e.g., at $t_1 + 96$ s in Fig. 3a (Supplementary Movie 4). Note that, occasional failures of ice bridging also appeared during the freezing wave propagation on a flat surface, which did not prevent the ice bridge connection from invading the whole surface in a chain reaction fashion (Supplementary Movie 3).

Previous research has shown that the local inter-droplet ice bridge connection is related to the inter-droplet configuration[21,31,40] and the detailed analysis is given in Supplementary Note 4 and Supplementary Movie 5. To understand the reason why the failures of the ice bridge connection are massively present on the macro-ridged surface as shown in Fig. 3a, we first consider the droplet distribution on the surface. The first panel in Fig. 3c shows that the condensate droplets distributed in a gradient manner with the bigger ones farther away from the ridge, and the inter-droplet distance increases as the droplets size decreases, all of which results in a droplet coverage
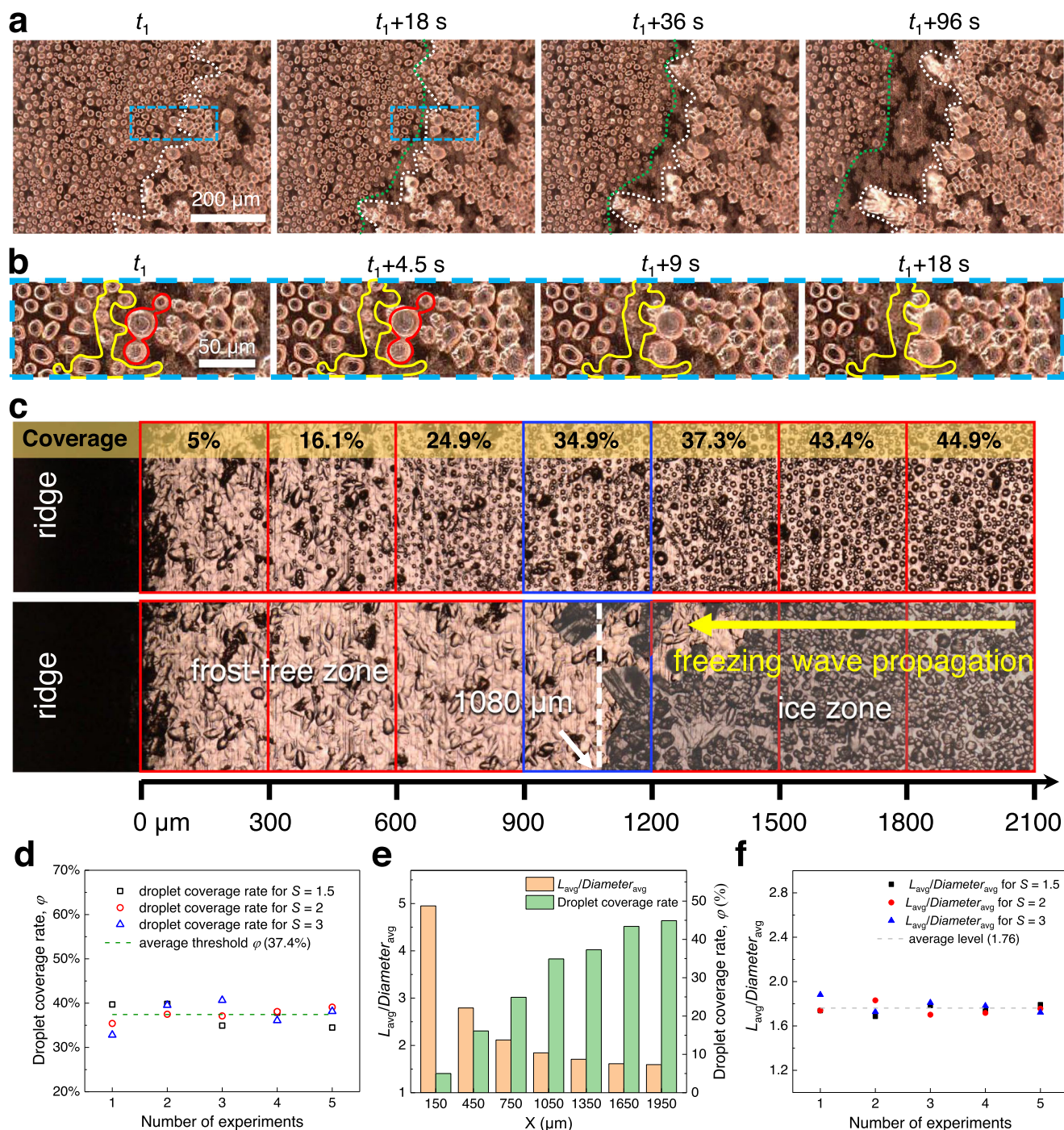
Fig. 3 Failure of ice bridge connection on the macro-ridged surface. a Time-lapse images showing the formation of frost-free zone boundary. **b** Enlarged partial view showing the details for the failure of inter-droplet ice bridging. Droplets circled in red froze while in yellow evaporated completely. **c** Division of the surface area for the analysis of droplet coverage rate obtained from Supplementary Figs. S9c, d. The first row shows the droplet distribution just before freezing, while the second one with the ice zone covered by gray shadow shows the formed frost-free zone after freezing. The white dotted line indicates the boundary between the frost-free zone and ice zone. **d** Droplet coverage rate at the region where the freezing wave propagation terminated at different supersaturation levels. **e** Bar graph for $L_{avg}/Diameter_{avg}$ and the droplet coverage rate of each region in **c**, and the position of each column corresponds to the center coordinates of each region. **f** $L_{avg}/Diameter_{avg}$ for the regions in **d** where numerous failures of ice bridging occurred.

gradient. This is in contrast to the case on a flat surface that the droplets distribute uniformly and close to each other, providing multiple paths for ice bridge connection despite occasional failures (Supplementary Movie 3). Therefore, we speculate that there would be a critical droplet size and inter-droplet distance, which can be reflected by the droplet coverage rate, for numerous failures of ice bridge connection.

For simplicity, as shown in Fig. 3c, we divided the condensation strip into several regions, e.g., with an equal spacing of 300 μm, considering a reasonable trade-off between accuracy and efficiency in data processing. For $S = 2$, the corresponding boundary separating frost-free zone from ice zone is located at ~1080 μm as indicated by the white dotted line, namely, numerous failures of ice bridge connection occurred around this

position. Note that, the freezing wave spreads from the edges of the surface to the ridge corner, indicating the ice bridging initiates from regions with a large droplet coverage rate and propagates towards the regions with a small one, as indicated by the yellow arrow. By analyzing the droplet coverage rate for the region where the freezing wave propagation terminated, i.e., the boundary, at different supersaturation levels (Supplementary Note 5 and Supplementary Fig. 9), we find that the droplet coverage rate for these regions keeps an almost constant value. As shown in Fig. 3d, 15 sets of statistical results of droplet coverage rate for the regions that the ice propagation terminated, yield an average threshold droplet coverage rate at ~37%. This means that numerous ice bridge failures can be triggered when the droplet coverage rate is less than 37%. In other words, ice bridge connection succeeds when the droplet coverage rate of the surface is larger than 37%.

In order to reveal the specific inter-droplet configuration for numerous failures of ice bridging, we analyze the ratio of the average distance between droplets L_{avg} and average droplet diameter $Diameter_{avg}$ in each region for $S = 2$ (Fig. 3c), as well as the other supersaturation levels (Supplementary Note 6 and Supplementary Figs. 10 and 11). As shown in Fig. 3e, $L_{avg}/Diameter_{avg}$ decreases dramatically as the φ increases, indicating that regions with higher coverage have a denser droplet distribution. Compared with the droplet coverage rate, the dimensionless number $L_{avg}/Diameter_{avg}$ reflects more detailed information for the inter-droplet configuration, which can be considered as a modified form of bridging parameter S^* as used in previous research[21,26]. Since there exists a critical value of S^* for the ice bridge failed to connected its target droplet, a critical value of $L_{avg}/Diameter_{avg}$ is expected for numerous failures of ice bringing among multiple droplets. After calculating 15 sets of $L_{avg}/Diameter_{avg}$ for the regions where numerous failures of ice bridging occurred, i.e., the regions used in Fig. 3d, an average $L_{avg}/Diameter_{avg} = 1.76 \pm 0.05$ was obtained, as shown in Fig. 3f, indicating that numerous ice bridge failures for multiple droplets can be triggered when the inter-droplet configuration $L_{avg}/Diameter_{avg}$ is greater than ~1.76. Furthermore, we find that the gradient distribution of droplets contributes greatly to the stability of the anti-icing performance. Specifically, the gradient droplet distribution on the surface with a macro-ridge slows down the freezing wave propagation (Supplementary Note 7), and the formation of the frost-free zone is hardly affected by the nucleation position (Supplementary Note 8).

Anti-icing performance of the macro-ridge arrayed surface. Single macro-ridge on the surface serves as a necessary pre-requisite for the frost-free zone formation, and predicting frost proportion on surfaces with periodic ridge arrays is also highly important for anti-icing applications in many practical scenarios. For this purpose, we first consider the frost-free area proportion f on the surface with single macro-ridge. Figure 4a shows that the simulated critical f for dry-zone formation decreased along with the increasing ridge width D, which agrees well with the experimental results. Note that, for a given ridge height, e.g., $H = 3$ mm, different ridge width D corresponds to different critical f and then different L could be calculated accordingly (Fig. 1g). As depicted in Fig. 4b, it's reasonable that an equal P and L could render the bottom surface between the ridges frost free on the macro-ridge arrayed surface, on which the frost-free area proportion f is the same as that on the single macro-ridged surface.

Accordingly, one might think that the minimized D, e.g., 0.1 mm, should be chosen to design the arrayed surface in order to achieve the largest frost-free area proportion ~97% (Fig. 4a). However, the following factors need to be considered: the

structure with a small feature size would not only deteriorate the mechanical properties of the surface, but also cause numerous manufacturing challenges as the total surface area increased dramatically. Figure 4c discussed the tradeoff between the frost area proportion $(1 - f)$ and the dimensionless surface area defined as $\eta = A_{ridge}/A_{flat}$, where $A_{ridge} \sim \pi D/2 + 2(H - D) + L$ represents the surface area for one unit, signified by the red zone (Fig. 4b), and $A_{flat} \sim L$ represents the surface area for a flat surface without ridge. The frost area proportion increases along with the increasing ridge width, while the dimensionless surface area η decreases dramatically. Therefore, an optimum regime emerges around $D \approx 1$ mm at which an optimal balance can be achieved, and the ridge pitch can be derived as $P = L = D/(1 - f) \approx 3.85$ mm with $f_{D=1} \sim 74\%$. Similarly, the optimized $H = 3$ mm is discussed in Supplementary Note 9. Note that, a prediction of $P \approx 4.1$ mm is made by considering the balance between the incoming and outgoing vapor flux at the inter-mediate areas between two adjacent ridges on the H3D1 surface (Supplementary Note 10). Based on above analysis, an approx-imate value of $P = 4$ mm is chosen for the surface design. In other words, $P = 4$ mm is a critical ridge pitch to keep the intermediate areas between the ridges frost free under the corresponding experimental conditions, and otherwise frost can invade the intermediate areas of the macro-ridge arrayed surface with a larger pitch value. This is verified by the experiments under the conditions $S = 2$, $T_w = -7$ °C and $RH = 31\%$ on the surface with the macro-ridged arrays with $P = 4$ mm and 5 mm, respectively (Fig. 4d). More results with different experimental conditions are given in Supplementary Table 2. It shows that the intermediate areas between two ridges keep frost free for $P = 4$ mm while frost forms for $P = 5$ mm in most cases.

To further validate the anti-frosting performance of the designed surface with $H = 3$ mm, $D = 1$ mm and $P = 4$ mm (H3D1P4), condensation frosting experiments under different supersaturation levels are carried out, and the results are compared with previous work, as shown in Fig. 4e. Note that, a projected frost-free area proportion f_p on the surface is defined because a long-period frost accumulation would shield part of the frost-free area from the top view. It is obvious that the fabricated surface possesses a larger projected frost-free area proportion than that reported by Ahmadi et al.[32], despite almost twice the supersaturation level in our case. Note that, a high f_p was observed for the initial stage[32], which is attributed to the pre-deposited ice stripes of ~100 μm. In addition, $S = 1.1$ is a weak supersaturation under which subcooled droplets hardly nucleat-ing in our experiment, and therefore we chose $S = 1.5$ as the lower limit of supersaturation level for a natural condensation frosting. Moreover, even though in such a weak supersaturation level of $S = 1.1$, in the first 8 h, the frost growth rate of surface designed by Ahmadi et al. is more than sixfold the growth rate compared to ours with the supersaturation level $S = 1.5$, which may be attributed to the enhanced vapor diffusion flux by the sharp-top ridge with a width of 100 μm[37]. This means that though micro-scale ridge may realize a large frost-free area proportion by sacrificing its extreme narrow top part at the initial frosting stage, the high growth rate of frost makes it uncompe-titive in a long period. For experiments with extreme super-saturation level $S = 3$, our results show a much larger frost-free area proportion, which is far superior to that on the macro-serrated surface as discussed by Yao et al.[35]. The anti-frosting performance of the surface with macro-ridged arrays was further demonstrated by an impressive durable frosting experiments, e.g., 48 h. As shown in Fig. 4f, the surface could keep a frost-free area proportion as high as ~43% in 24 h and ~29% in 48 h with the supersaturation level $S = 2$, which makes it outstanding among the many existing anti-icing surfaces.
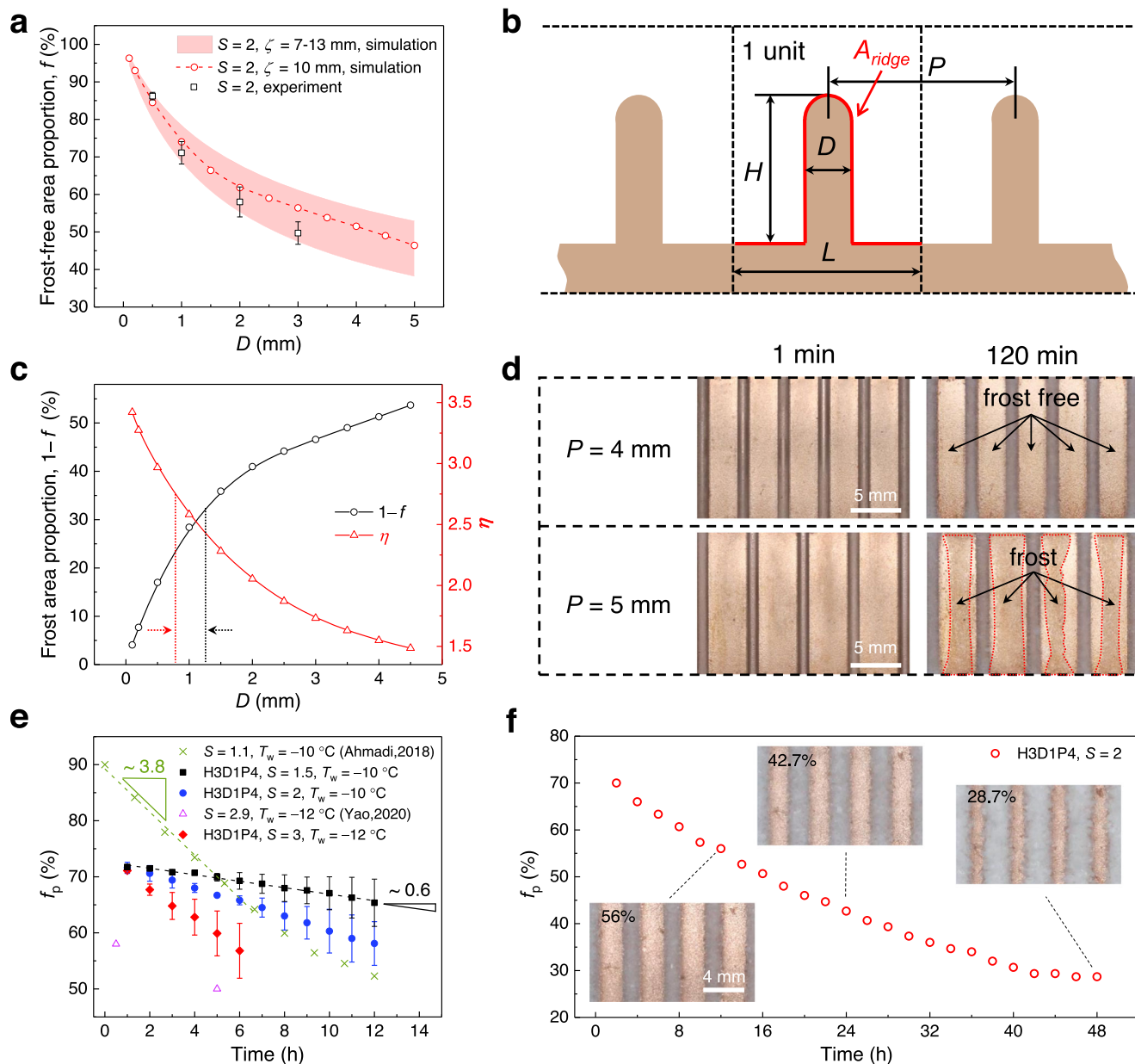
Fig. 4 Frosting on the macro-ridge arrayed surface. a Frost-free area proportion as a function of ridge width D on the surface with single ridge. The pink band represents the simulated results using the boundary layer thickness ranging from 7 mm to 13 mm. The experimental f are obtained at one hour after the experiment begins (Supplementary Fig. S14), and all results are repeated for three times. **b** Schematic showing the structure parameters of the macro-ridged array surface. **c** Influence of frost area proportion ($1-f$) and dimensionless surface area (η) changed with the ridge width D. **d** Experimental results on the macro-ridge arrayed surface with $P = 4$ mm and 5 mm, respectively, under $S = 2$ and $T_w = -7\,°C$. **e** Experimental results on the macro-ridge arrayed surface H3D1P4 under different supersaturation levels for 12 h. **f** Verification of the anti-frosting performance on the macro-ridged array surface H3D1P4 under $S = 2$ and $T_w = -10\,°C$ for 48 h. The error bars denote the standard deviation from three measurements.

Conclusion

In conclusion, we established a mechanistic paradigm for frost-free zone formation. We show that a macroscale ridge on the surface redistributes the condensates by changing the vapor diffusion flux during the condensation process, resulting in a gradient arrangement of condensate droplets according to their size. This unique droplet distribution subsequently enables numerous failures of ice bridge connection at the area with a critical droplet coverage rate, to generate a boundary separating the dry zone from the ice zone. Then a frost-free zone forms around the ridge corner after the rest droplets evaporate completely, which is attributed to the dominated outgoing vapor flux caused by the hygroscopicity of ice. Moreover, macro-ridge arrayed surfaces are

designed to achieve an overall anti-frosting performance, compared to a small area of frost-free zone produced on the surface with a single macro-ridge. We envision that this fundamental understanding of frost-free zone formation and the corresponding anti-frosting strategy might open up a new avenue for the development of anti-icing surfaces in various applications where a long-term resistance to frost/ice accretion is required.

Methods

Sample preparation. In the condensation frosting experiments, T2 copper plate was chosen for the surface preparation due to its high thermal conductivity. Specifically, the macro-ridged surfaces were first fabricated using a wire-cutting machine, followed by polishing with a magnetic grinding machine for 30 min. The

samples were then ultrasonically cleaned in ~1 M hydrochloric acid solution and deionized water for 3 min and 5 min, respectively. The surface roughness was measured by a 3D optical surface profile (NewView^{TM} 9000, Zygo) to be Sa ~ 0.3 μm, as shown in Supplementary Fig. 1.

The control of temperature and humidity. As shown in Fig. 1c, the vapor temperature and humidity in the chamber are detected by the humidity sensor, and the humidity is controlled by humid/dry air discharging through a humidity tube with a controller (Linkam, RH95). The surface temperature is precisely regulated by a Peltier cold stage with a temperature sensor and a digital temperature controller. The sample was taped on a Peltier cold stage by a double-side copper tape (3M 1182, 18 mm wide and 0.04 mm thick) to ensure a stable heat conduction during the experiment.

Experimental setup. A customized transparent PMMA chamber (15 cm × 12 cm × 7 cm, L × W × H) was used to endow a stable ambient condition over the surface. The surface was covered by a plastic film to prevent the humid air from condensing before the surface temperature as well as the humidity and temperature of ambient air were stabilized. After all the factors are stable, e.g., $T_w = -7 \pm 0.1$ °C, $T_{air} = 20 \pm 0.1$°C and RH = 31%, corresponding to the supersaturation level $S = 2$ (see Supplementary Note 3 for detailed calculation), the plastic film was removed gently and quickly, and then the condensation frosting process was recorded by a digital SLR camera (EOS 5D MarkIV, Cannon) with a macro lens (Canon EF 100 mm f/2.8L IS USM Macro Lens).

Method for droplet statistical analysis. The data of droplet coverage in Fig. 2c are extracted from the counting statistics of droplets in Fig. 1f. Specifically, micrographs during droplet condensation on the macro-ridged surface were snapshotted using a digital microscope (VHX-900F, Keyence) when the condensation process was stable. Then the pixel-counting software ImageJ was used to stitch the micrographs together to form Fig. 1f. The counting masks circling the droplets greater than 4 pixels are shown as the green circles in Supplementary Fig. 6, and thus the area and centroid coordinates of each droplet can be further analyzed by ImageJ. 14 equal regions were divided, and the data of the corresponding droplet coverage in each region was presented in Fig. 2c.

Data availability

The data that support the findings of this study have been included in the manuscript and supplementary information. Any additional data are available from the corresponding author upon reasonable request.

References

1. Stone, H. A. Ice-phobic surfaces that are wet. *ACS Nano* **6**, 6536–6540 (2012).
2. Parent, O. & Ilinca, A. Anti-icing and de-icing techniques for wind turbines: critical review. *Cold Reg. Sci. Technol.* **65**, 88–96 (2011).
3. Laforte, J. L., Allaire, M. A. & Laflamme, J. State-of-the-art on power line de-icing. *Atmos. Res.* **46**, 143–158 (1998).
4. Lv, J. Y., Song, Y. L., Jiang, L. & Wang, J. J. Bio-inspired strategies for anti-icing. *ACS Nano* **8**, 3152–3169 (2014).
5. Kreder, M. J., Alvarenga, J., Kim, P. & Aizenberg, J. Design of anti-icing surfaces: smooth, textured or slippery? *Nat. Rev. Mater.* **1**, 15003 (2016).
6. Yang, S. Y. et al. Condensation frosting and passive anti-frosting. *Cell Rep. Phys. Sci.* **2**, 100474 (2021).
7. Golovin, K. et al. Designing durable icephobic surfaces. *Sci. Adv.* **2**, e1501496 (2016).
8. Golovin, K., Dhyani, A., Thouless, M. D. & Tuteja, A. Low-interfacial toughness materials for effective large-scale deicing. *Science* **364**, 371–375 (2019).
9. Shrestha, B., Ezazi, M., Rad, V., Maharjan, A. & Kwon, G. Frost delay of a water-absorbing surface with engineered wettability via nonfreezing water. *Langmuir* **38**, 5787–5794 (2022).
10. Chatterjee, R., Bararnia, H. & Anand, S. A family of frost-resistant and icephobic coatings. *Adv. Mater.* **34**, 2109930 (2022).
11. Kota, A. K., Kwon, G. & Tuteja, A. The design and applications of superomniphobic surfaces. *NPG Asia Mater.* **6**, e109 (2014).
12. Lafuma, A. & Quéré, D. Superhydrophobic states. *Nat. Mater.* **2**, 457–460 (2003).
13. Varanasi, K. K., Deng, T., Smith, J. D., Hsu, M. & Bhate, N. Frost formation and ice adhesion on superhydrophobic surfaces. *Appl. Phys. Lett.* **97**, 234102 (2010).
14. Wang, Y. Y., Xue, J., Wang, Q. J., Chen, Q. M. & Ding, J. F. Verification of icephobic/anti-icing properties of a superhydrophobic surface. *ACS Appl. Mater. Interfaces* **5**, 3370–3381 (2013).
15. Wong, T. S. et al. Bioinspired self-repairing slippery surfaces with pressure-stable omniphobicity. *Nature* **477**, 443–447 (2011).
16. Kim, P. et al. Liquid-infused nanostructured surfaces with extreme anti-ice and anti-frost performance. *ACS Nano* **6**, 6569–6577 (2012).
17. Wilson, P. W. et al. Inhibition of ice nucleation by slippery liquid-infused porous surfaces (slips). *Phys. Chem. Chem. Phys.* **15**, 581–585 (2013).
18. Stamatopoulos, C., Hemrle, J., Wang, D. & Poulikakos, D. Exceptional anti-icing performance of self-impregnating slippery surfaces. *ACS Appl. Mater. Interfaces* **9**, 10233–10242 (2017).
19. Rykaczewski, K., Anand, S., Subramanyam, S. B. & Varanasi, K. K. Mechanism of frost formation on lubricant-impregnated surfaces. *Langmuir* **29**, 5230–5238 (2013).
20. Irajizad, P., Hasnain, M., Farokhnia, N., Sajadi, S. M. & Ghasemi, H. Magnetic slippery extreme icephobic surfaces. *Nat. Commun.* **7**, 13395 (2016).
21. Boreyko, J. B. & Collier, C. P. Delayed frost growth on jumping-drop superhydrophobic surfaces. *ACS Nano* **7**, 1618–1627 (2013).
22. Chen, X. M. et al. Activating the microscale edge effect in a hierarchical surface for frosting suppression and defrosting promotion. *Sci. Rep.* **3**, 2515 (2013).
23. Hao, Q. et al. Mechanism of delayed frost growth on superhydrophobic surfaces with jumping condensates: more than interdrop freezing. *Langmuir* **30**, 15416–15422 (2014).
24. Jung, S., Tiwari, M. K., Doan, N. V. & Poulikakos, D. Mechanism of supercooled droplet freezing on surfaces. *Nat. Commun.* **3**, 615 (2012).
25. Zhang, Q. L. et al. Anti-icing surfaces based on enhanced self-propelled jumping of condensed water microdroplets. *Chem. Commun.* **49**, 4516–4518 (2013).
26. Chatterjee, R., Beysens, D. & Anand, S. Delaying ice and frost formation using phase-switching liquids. *Adv. Mater.* **31**, e1807812 (2019).
27. He, Z. Y. et al. Bioinspired multifunctional anti-icing hydrogel. *Matter* **2**, 723–734 (2020).
28. Dooley, J. B. *Determination and characterization of ice propagation mechanisms on surfaces undergoing dropwise condensation.* Ph.d. diss., (Texas A& M University, 2010).
29. Guadarrama-Cetina, J., Mongruel, A., Gonzalez-Vinas, W. & Beysens, D. Percolation-induced frost formation. *Europhys. Lett.* **101**, 16009 (2013).
30. Murphy, D. M. & Koop, T. Review of the vapour pressures of ice and supercooled water for atmospheric applications. *Q. J. R. Meteorol Soc.* **131**, 1539–1565 (2005).
31. Nath, S. & Boreyko, J. B. On localized vapor pressure gradients governing condensation and frost phenomena. *Langmuir* **32**, 8350–8365 (2016).
32. Ahmadi, S. F. et al. Passive antifrosting surfaces using microscopic ice patterns. *ACS Appl. Mater. Interfaces* **10**, 32874–32884 (2018).
33. O'Brien, J. L. et al. Spatial control of condensation and desublimation using ice nucleating proteins. *Appl. Phys. Lett.* **113**, 153701 (2018).
34. Jin, Y. K. et al. Inhibiting condensation freezing on patterned polyelectrolyte coatings. *ACS Nano* **14**, 5000–5007 (2020).
35. Yao, Y. H. et al. Frost-free zone on macrotextured surfaces. *Proc. Natl. Acad. Sci. USA* **117**, 6323–6329 (2020).
36. Miljkovic, N. et al. Jumping-droplet-enhanced condensation on scalable superhydrophobic nanostructured surfaces. *Nano Lett.* **13**, 179–187 (2013).
37. Park, K.-C. et al. Condensation on slippery asymmetric bumps. *Nature* **531**, 78–82 (2016).
38. Beysens, D. Dew nucleation and growth. *C. R. Phys.* **7**, 1082–1100 (2006).
39. Zhao, Y. J. et al. Effects of millimetric geometric features on dropwise condensation under different vapor conditions. *Int. J. Heat Mass Transf.* **119**, 931–938 (2018).
40. Nath, S., Ahmadi, S. F. & Boreyko, J. B. How ice bridges the gap. *Soft Matter* **16**, 1156–1161 (2020).

Acknowledgements

Author contributions

Y.L. and C.Lu. conceived the research. Y.L. supervised the research. C.Lu. and C.L. performed the experiments. C.Lu. performed the simulations with the help from Z.Y. and L.Z. C.Lu. analyzed the data with contributions from H.Z., L.Z. and S.F. Y.L. and D.Z. provided technical guidance in various aspects of the project. C.Lu. and Y.L. wrote the manuscript. All authors reviewed the manuscript.

Competing interests

The authors declare no competing interests.

Additional information

Supplementary information The online version contains supplementary material available at https://doi.org/10.1038/s43246-022-00308-5.

Correspondence and requests for materials should be addressed to Yahua Liu.

Peer review information *Communications Materials* thanks Yugang Zhao and the other, anonymous, reviewers for their contribution to the peer review of this work. Primary Handling Editor: John Plummer.

Reprints and permission information is available at http://www.nature.com/reprints

Publisher's note Springer Nature remains neutral with regard to jurisdictional claims in published maps and institutional affiliations.